Observation and analysis of emergent coherent structures in a high-energy-density shock-driven planar mixing layer experiment

F. W. Doss,* K. A. Flippo, and E. C. Merritt
Los Alamos National Laboratory, Los Alamos, New Mexico 87545, USA
(Received 19 February 2016; revised manuscript received 8 July 2016; published 3 August 2016)

Coherent emergent structures have been observed in a high-energy-density supersonic mixing layer experiment. A millimeter-scale shock tube uses lasers to drive Mbar shocks into the tube volume. The shocks are driven into initially solid foam (60 mg/cm^3) hemicylinders separated by an Al or Ti metal tracer strip; the components are vaporized by the drive. Before the experiment disassembles, the shocks cross at the tube center, creating a very fast ($\Delta U > 200$ km/s) shear-unstable zone. After several nanoseconds, an expanding mixing layer is measured, and after 10+ ns we observe the appearance of streamwise-periodic, spanwise-aligned rollers associated with the primary Kelvin-Helmholtz instability of mixing layers. We additionally image roller pairing and spanwise-periodic streamwise-aligned filaments associated with secondary instabilities. New closures are derived to connect length scales of these structures to estimates of fluctuating velocity data otherwise unobtainable in the high-energy-density environment. This analysis indicates shear-induced specific turbulent energies 10^3–10^4 times higher than the nearest conventional experiments. Because of difficulties in continuously driving systems under these conditions and the harshness of the experimental environment limiting the usable diagnostics, clear evidence of these developing structures has never before been observed in this regime.

DOI: 10.1103/PhysRevE.94.023101

I. INTRODUCTION

Plane shear layers, consisting of parallel streams of fluids with different velocities and perhaps different compositions, have been long been studied as a canonical flow leading to instability [1] and subsequent turbulent mixing of mass and momentum across the fluid interfaces [2,3]. Experiments have investigated the scaling of layer behavior with variations in flow velocity [4], density [5], and compressibility [6,7], and have elucidated the mechanisms by which primary instability structures interact and drive the system toward three dimensionality [8–13]. The data from such experiments have been used to calibrate and test engineering models for practical flows [14–16] which are increasingly extended for use in design and interpretation in physics, including inertial confinement fusion experiments [17,18] and astrophysics [19].

In this paper, researchers from Los Alamos National Laboratory (LANL) report results from a high-energy-density (HED) shock-driven shear experiment in which two equal-strength shocks, separated by a thin metal foil, are sent streaming past each other in a laser-driven shock tube. Where the shocks cross, a very strong shear instability is initiated. The foil is mixed into the surrounding material, and the system becomes a temporally growing mixing layer. Twenty nanoseconds after the onset of shear, the tube disassembles and the experiment ends, but before that time signs of the evolving mixing layer are observed and recorded by x-ray radiography. For the first time in an HED system, this has included finding coherent structures associated with the primary and secondary instabilities of a mixing layer. Geometrically, this experiment is in the families of counterflowing mixing layer experiments (such as the experiments by Papamoschou [20] or Alvi *et al.* [21]) and of supersonic variable-density shear experiments (with examples including Ninnemann and Ng [22] and Strykowski and Niccum [23]), arranged here with a layer of high density initially present between two fast, counterflowing, low-density streams.

By observing in our experiment the appearance of classical shear structures similar and clearly closely related to those in the aforementioned class of traditional mixing layer experiments [5,10], we establish the preservation of hydrodynamic scaling principles across more than 8 orders of magnitude in time and velocity and establish a system where, going forward, these plasma experiments can be analyzed and interpreted in the context of the large body of existing work on planar mixing layer phenomenology.

HED physics experiments, referring by convention to experiments in which the typical energy density exceeds about 100 kJ/cm^3 (for a stationary fluid element, this is an equivalent pressure of 10^6 atmospheres), have been used to investigate the extrapolation of fluid mechanics into novel physics regimes. Because the pressures and temperatures involved typically represent energy densities exceeding those of chemical or mechanical reactants by many orders of magnitude, one method of driving the experiments is by using pulsed laser facilities which optically focus light to high intensities (>1 TW/mm^2). Because of the impulsive and unsustainable nature of this drive, the experiments typically feature and explore shocks and other transient phenomena. Overviews of the chief physics of interest in this regime can be found in the classic monograph by Zeldovich and Razier [24] and in more recent books by Atzeni and Meyer-ter-Vehn [25], Drake [26], and Colvin and Larsen [27].

Many HED experiments focus on the linear and early nonlinear growth phases of shock-initiated instabilities, particularly under extended physics regimes such as coupled radiation-hydrodynamics or convergent geometries, due to their relevance to the late-time evolution of inertial fusion capsules and to astrophysical systems [28]. Because of the impulsive nature of the drive, the experiments usually either do not reach or are not able to diagnose the deeply nonlinear

*fdoss@lanl.gov

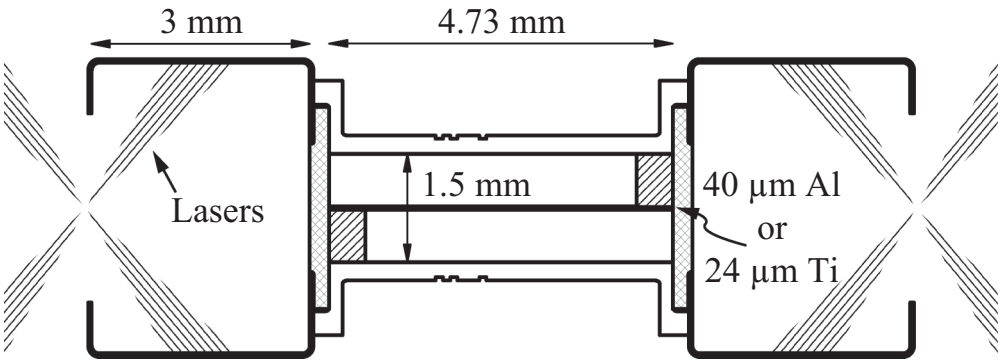

FIG. 1. Schematic of the LANL HED shear experiment. Laser light shines into the target from the left and right, creating a radiation field which vaporizes part of the crosshatched plastic ablator to drive shocks into the beryllium shock tube.

or turbulent regimes. These experiments do have advantages when machining initial conditions, since the materials can all be prepared in the solid phase and have accordingly been used to study single-mode evolution of Rayleigh-Taylor and similar instabilities; examples spanning several generations of laser facilities include Cole *et al.* [29], Glendinning *et al.* [30], Robey [31], and Kuranz *et al.* [32] using planar targets, and Wark *et al.* [33] and Raman *et al.* [34] in converging geometries. Other HED shear instability experiments have also been performed, including early experiments by Hammel *et al.* [35], single-mode single-sided blast-wave-driven experiments described by Hurricane and Harding [36,37], more steadily driven single-sided experiments by Di Stefano *et al.* [38] and Wan *et al.* [39], and two-stream experiments by Welser-Sherrill *et al.* [40] driven by two coflowing shocks of unequal speeds on each side. However, all of these experiments, driven by shocks from only one side, develop considerable pressure gradients across the mixing interface, adding confounding dynamics apart from those of pure shear flow. Furthermore, while a later variation of the Hurricane-Harding experiment without the sinusoidal seed was described as developing a mixing region consistent with a Reynolds-averaged computational model calculation [41–43], no coherent structures associated with shear were observed.

Our data are ultimately intended for use in benchmarking models of variable-density turbulence [44] as compressibility, very-high-density-ratio interfaces, and plasma physics effects become important in inertial-fusion-relevant regimes. To that end, exploratory studies in these and other parameters are in progress. The effects of highly variable density flow have only relatively recently begun to be incorporated into engineering models for turbulent flow, and while modeling the effects of buoyancy-driven instabilities has been studied in depth [45–49], modeling compressible and multimaterial flows under shear is still in an early phase. Work applying such models to experiments with typical gas-phase density ratios has been performed [50,51], but the HED environment additionally allows for an extremely wide range of initial densities as well as fine control over the initial material interfaces.

II. EXPERIMENTAL DESIGN

Figure 1 shows the geometry of the LANL HED shear experiment [52,53]. The experiment has a barbell-like geometry which launches collimated shocks from each side of the tube that cross and initiate shear at the tube center. The experiment was originally fielded at smaller scale and at lower energies using the OMEGA Laser System at the Rochester Laboratory for Laser Energetics [54], a 40-kJ laser facility. These experiments were successful [55–57] at fielding a smaller, prototype implementation of the counterflowing shear geometry in Fig. 1 but were not completely able to sustain it for long times, nor to isolate it from transients and outside influences long enough for classical shear flow structures to materialize.

The experiments were then expanded to larger dimensions and fielded at the National Ignition Facility (NIF) at Lawrence Livermore National Laboratory [58]. The NIF is a 2-MJ laser, optimized for the execution of indirectly driven, inertially confined fusion experiments [59]. In order to perform these experiments, which take place in gold cylinders called hohlraums, the beams are preferentially aligned to shine into laser entrance holes at the top and bottom of the hohlraum. The purpose of the gold hohlraum is to absorb laser light and reemit it as a high-temperature soft x-ray bath which, by vaporizing the outermost surface of the capsule, drives the subsequent hydrodynamics. This HED shear experiment, likewise, is fitted with gold hohlraums 3 mm tall on each side of a 5-mm-long beryllium shock tube. When the lasers heat these hohlraum volumes to radiation temperatures of 250 eV (2.9 million kelvin), ablation commences on the surface of the polystyrene endcaps, shown in crosshatch in Fig. 1. This then drives by reaction traveling shocks into the tube volume, estimated by simulation to be of strength 10 Mbar and to travel at 140 km/s through the tube interior. The distance between the endcaps inside the tube is 4.73 mm, from which the shocks are launched after 3 ns. Even before this has happened, high-energy components of the x-ray spectrum being emitted by the hohlraums have streamed through the tube, heating the components to tens of thousands of kelvin, into the plasma state. Gold hemicylindrical plugs are inserted into opposing corners of the tube, represented by single hatching in Fig. 1, which confine the launched shock to either the top or bottom half of the tube.

The tube volume is filled by a polystyrene (CH) foam initially of density 60 mg/cm^3. The tube is additionally bisected by a metal plate, which will serve both as a diagnostic tracer and as a collimator to keep each shock confined to its

TABLE I. Fluid parameters for different materials in the experiment: sound speeds c_s, Mach numbers of the 110 km/s boundary flow velocity, material viscosities ν, average ionization numbers Z, Atwood numbers with reference to the light CH foam, and Reynolds numbers defined in terms of both late-time integral scale (Re_L) and initial rms roughness amplitude (Re_0). Fluid viscosities ν are in cSt (mm^2/s). Sound speeds c_s are in km/s.

	c_s	M	ν	Z	At	Re_L	Re_0
Al	35	3.1	4	3	0.57	1.8×10^7	5×10^3
Ti	30	3.6	$\frac{1}{2}$	4.5	0.72	1.6×10^8	4×10^4
CH	66	1.7	12	4.5	0	N/A	N/A

own half for the early times of the experiment. The metal plate has so far been foils of either been 40-μm-thick aluminum or 24-μm-thick titanium, each at solid density. After about 18 ns, the shocks cross in the center of the tube. The center region of the tube is now experiencing a strong shear gradient across the metal plate, with postshock flow speeds of 110 km/s on each side of the layer for a total shear velocity difference across the layer of $\Delta U = 220$ km/s. Simulations with the LANL radiation-hydrodynamics code RAGE [60], which resolve the radiation drive, shocks, and the bulk hydrodynamics but not the small-scale features of the flow, suggest that the flow Mach number in the foam to each side of the layer is 1.5, with a density of 0.3 $\mathrm{g/cm}^3$ and a temperature of 50 eV, while the aluminum foil is around 1 $\mathrm{g/cm}^3$. The simulation uses the SESAME [61] equation of state database to infer the properties of these materials through the simulation. Table I records some fluid parameters and dimensionless number estimates for the aluminum and titanium experiments using plasma physics calculations described in Appendix A.

The metal foil is initially mostly at rest after shock crossing and achieves some gradient of velocity as time goes on. Of mechanisms discussed for the continued existence of Kelvin-Helmholtz instability under supersonic conditions [7], this experiment will clearly possess a subsonic core within the metal layer. The ongoing growth mechanisms of the layer, where they are strongly influenced by the high-density central region, may be modified from the usual case, though the same fundamental considerations are expected to apply.

The layer evolution is diagnosed by x-ray radiography, in which additional beams of the laser facility are used to heat an x-ray source (here, iron) which then sends x rays through the target volume and are imaged on film on the opposing side of the chamber. Since the x rays are preferentially absorbed by the atoms from the metal foil and are relatively unattenuated by either the beryllium shock tube or the light foam, the predominant feature in the images is the location and distribution of the metal foil material. The cameras integrate over 100 ps. More data on the specific diagnostic scheme implemented here is available in Flippo *et al.* [62]. In the early versions of this experiment, the shock tube was made of dense plastic but has since been replaced by beryllium for its superior x-ray transparency.

III. RADIOGRAPHY

X-ray images imaging both the mixing layer width and perpendicular to that view are recorded. Due to the short time scales of the experiment, typically only a few closely clustered images can be obtained in a single shot. The different times and directions of images shown then come mostly from different instances of the same target. The targets themselves are machined to high precision, with tolerances on critical parts in the range of 10 μm, and the variation of the laser drive from shot to shot is found to be within an acceptable range ($\leqslant 5\%$) to consider the different shots as separate realizations which can be combined into a common experimental result. NIF's shot identification numbers are of the form NYYMMDD, a year-month-day date code indicating when each shot was fired.

Data has been obtained for both aluminum and titanium foils. Figures 2(a)–2(c) show edge-on radiography obtained at 16.4, 28.5, and 34.5 ns after the lasers turned on. (Two images were obtained in each of shots N131115 and N141006; the other images at 17.6 and 33 ns are in Doss *et al.* [52].) From 16.4 ns to 34.5 ns, the layer grows from 146 μm to 377 μm in an average width sense. The layer was 40 μm wide at 0 ns. The first image at 16 ns shows the situation shortly before the shocks cross in the tube center. The shock locations can be inferred both from the deflection of the metal layer and, at the image top, the refraction of the shock into the tube wall. The last image shows most clearly what we are identifying as the formation of rollers in the mixing layer. Between these two images, one can observe that early in time the layer interface is smooth and sharply defined, while later in time the surface has become corrugated and appears more diffuse. One can also observe late in time the central section of tube where the shock strength was well balanced from top to bottom, and the metal layer remains linear. Off to the sides, the layer has obviously experienced some more complicated form of loading.

Figure 2(d) shows plan view measurements of the layer. This radiograph is taken perpendicular to the others, and the signal corresponds to differences in areal density of aluminum, which shows distinct streamwise-periodic features associated with Kelvin-Helmholtz rollers. In this view, we can see that the rollers stretch across the spanwise dimension of the tube and are clearly in possession of both curvature along their length and apparent points of approach where the vortex pairing instability will eventually effect a merger.

Experiments have also been performed in the titanium layer configuration. The 24-μm titanium foil is matched in mass to the 40-μm aluminum foil so that the initial response of the foil to the shocks will be similar in the two cases. The titanium layer both begins our extension to higher density ratios and simultaneously varies the initial foil thickness, testing the response of the instability to the initial geometry. Figure 3 shows edge-on and plan view radiography from titanium targets. The roller structures are less obvious in the edge-on view, but the plan view image at late time shows distinct spanwise features and mildly oblique ribs connecting them in the predominantly streamwise direction.

The edge-on views of the titanium configuration in Fig. 3 do not show as prominently the formation of roller structures as do those in Fig. 2 for the aluminum case. It is, however,

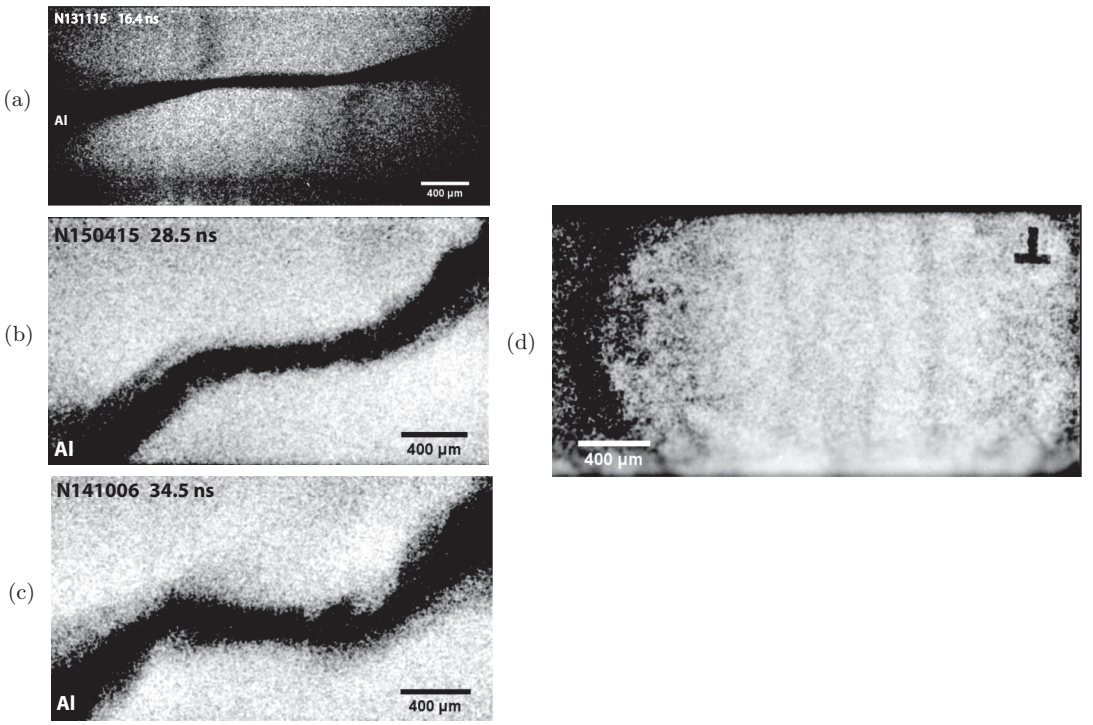

FIG. 2. Edge-on radiography from (a) N131115 at 16.4 ns, (b) N150415 at 28.5 ns, and (c) N141006 at 34.5 ns, and (d) plan radiography from N150527 at 30.5 ns. The ⊥ is an orientation fiducial on the film.

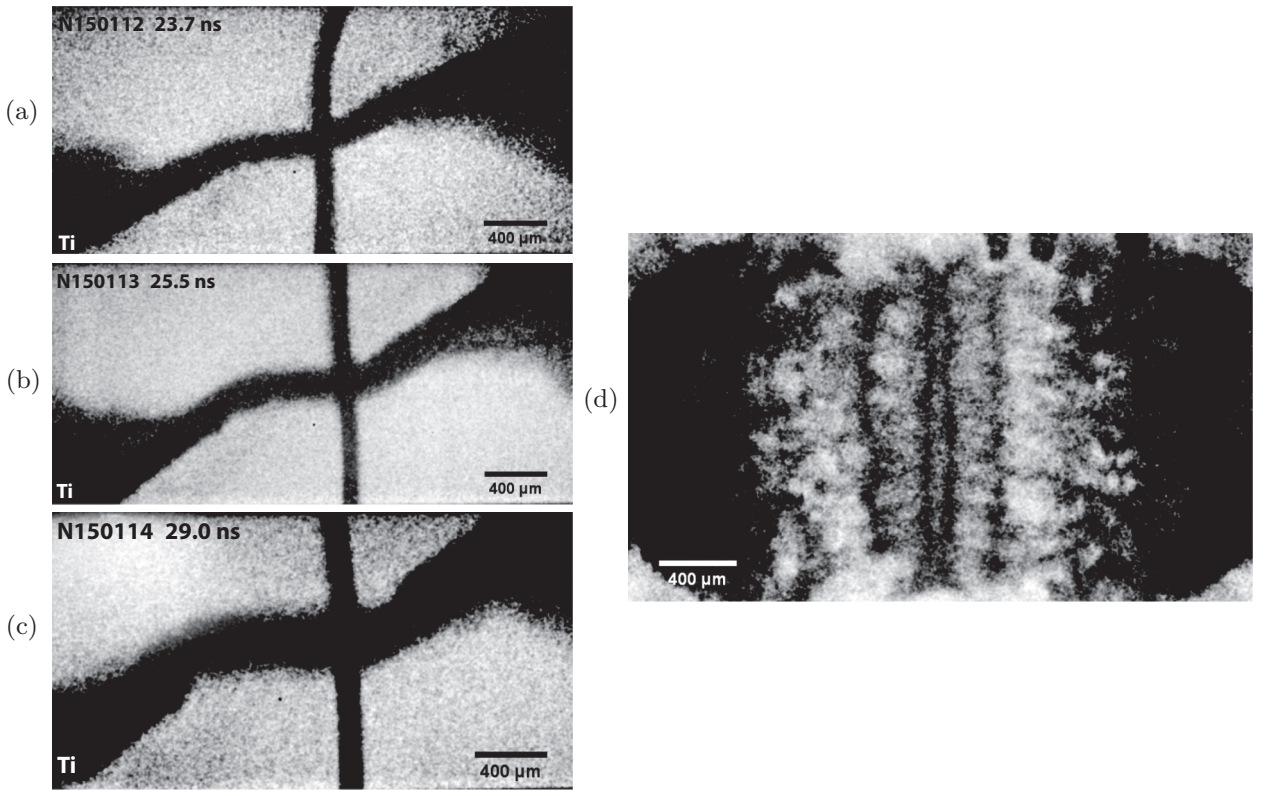

FIG. 3. Edge-on radiography from (a) N150112 at 23.7 ns, (b) N150113 at 25.5 ns, and (c) N150114 at 29 ns (the vertical line is a spatial fiducial wire outside of the shock tube), and also (d) plan radiography from N150604 at 34.5 ns.

best kept in mind that the edge-on views are integrated across the tube interior, and structures curved even a few degrees out of alignment with that direction will be averaged out in the final image. Figure 3(d) supports this interpretation, as it displays clear signs of spanwise-aligned, streamwise-periodic structures. Interestingly, the plan titanium view has some noticeable differences from the aluminum plan view. First, the streamwise periodicity seems to be more variable than in the aluminum, particularly with two filaments near the center appearing close together. The left-right symmetry of these structures still appears to be broadly preserved. It is possible that the titanium layer has been captured with the filaments near the center entering or exiting a recent merger. Second, running between the filaments we see what appear to be the spanwise-aligned, streamwise-periodic coherent structures sometimes called ribs.

These additional visible features in the titanium data may come both from enhanced diagnostic properties of the metal (titanium has higher opacity to the x rays used in the radiographic scheme than aluminum) leading to higher contrast, and from a more fully evolved mixing layer. All else being equal, dimensional analysis suggests the early layer evolution rates scale with $\Delta U/L$, where L is the initial thickness, so it is expected that the titanium layers (24 μm compared to 40 μm aluminum) may evolve further by the end of the experiment. Due to a plasma physics effect involving the different arrangement of electrons (see Appendix A), titanium also has a significantly lower viscosity than aluminum, which may contribute to faster evolution.

IV. ANALYSIS

The radiographic data in Figs. 2 and 3 are analyzed to ascertain properties of the mixing layer. Figure 4 shows representative lineouts measured to the left and right of a roller of interest, and streamwise from left to right across the shock tube. The spanwise lineouts are integrated in the streamwise direction by one resolution element (32 μm); the streamwise lineout is integrated across the central 500-μm span of the image. Lineouts were filtered with the 32-μm resolution by a rolling average, and noise is locally derived from the spread of values within each averaged element. Local transmission minima in the signal are identified with vortex locations if the minima are separated by at least one 32-μm resolution element and if the prominence of the intermediate peaks exceeds 44% of the local standard statistical deviation of the signal. (This discards minima without at least a 2/3 chance of being physically significant, and when used consistently across all lineouts resulted in the lowest global uncertainty for the combined data set.) Details of the other lineouts from the aluminum and titanium data are discussed in Appendix B.

Since our radiography is obtained by line-integrated x-ray transmission through the target, the plan view in particular cannot distinguish between structures on the top or bottom of the layer. Similarly, in the edge view, modulations of the layer material are integrated over the entire spanwise extent of the layer and become invisible if they are not coherent along the spanwise direction. This could lead, for example, to a misinterpretation of the mixing layer in aggregate as broader and more diffuse than perhaps it is at any particular point, if the height of the layer is highly modulated in the spanwise direction (to which the plan view would be insensitive to the sign of the displacement but may be able to detect the boundaries of such regions through limb-darkening effects).

We wish to extract as much information as possible, including flow parameters not directly observable by radiography, from measurements of the coherent structures. For decades substantial research efforts have investigated the nature of the emergent coherent structures of a mixing layer [9–13] and have associated these structures with flow parameters which could be straightforwardly measured in the conventional experiments. We plan to use these relations to infer fluctuation velocity information from the structures visible in the radiograph. Length scales of coherent flow structures will be extracted from the plan radiography. We measure first the coherent roller spacing a, from which one finds the circulation of the vortices, Reynolds numbers, and, from first-generation rollers, the wavelength of the principal Kelvin-Helmholtz instability, and second, the length scales b of the spanwise structures, which contain information related to the secondary instabilities which generate them. These will be analyzed in the framework of the elliptical instability [63–68] to infer information about the vortex structure of the rollers and the turbulent velocity fluctuations in the material.

A. Streamwise structure

The aluminum plan data at 30.5 ns [Fig. 2(d)] is used for an analysis of roller length scale and its consequences, since the roller filaments are roughly periodic. A roller periodicity a of $240 \pm 13\,\mu$m is observed in the aluminum. This can be used to infer roller circulation Γ, as far from the mixing layer the velocities in the streamwise direction are related by $\Delta U = \frac{\Gamma}{a}$. We will use the shearing velocity difference $\Delta U = 220$ km/s estimated by simulation as described above. This implies a circulation in each vortex of $\Gamma = 53 \times 10^3\ \mu\text{m}^2/\text{ns}$. Using our previous calculations in Table I for an aluminum plasma viscosity of 4 centistokes (cSt), we can also use this value to estimate an instantaneous Reynolds number of $\text{Re} = \Gamma/\nu = 1.3 \times 10^7$. This estimate lies between the two bounding Reynolds numbers in Table I and is well above estimates of the turbulent mixing transition criterion [69].

The corresponding titanium image [Fig. 3(d)] is much less periodic but will also be analyzed. From outside to center, we see roller spacings of first about 353 μm, then 225 μm, and finally at the center a spacing of 107 μm. The initial thickness of the titanium was 24 μm, 60% that of the 40-μm aluminum. Assuming the roller spacing derives its length scale from the initial foil thickness, the 107-μm spacing would naturally correspond to the rollers formed from the most unstable mode in the titanium, which here is still visible in the center of the plan view image. Taking this interpretation, this implies that the modes form first on the edges of the shock tube as the shocks enter and that the edges of the tube have experienced more shear-driven growth time for the various instabilities and hydrodynamic effects. The larger spacings to the left and right of the shock tube would correspond to rollers which have grown in size, presumably by amalgamation of the fundamental vortices. However, the corners, visible in the edge view, bounding the central, pressure-balanced, and

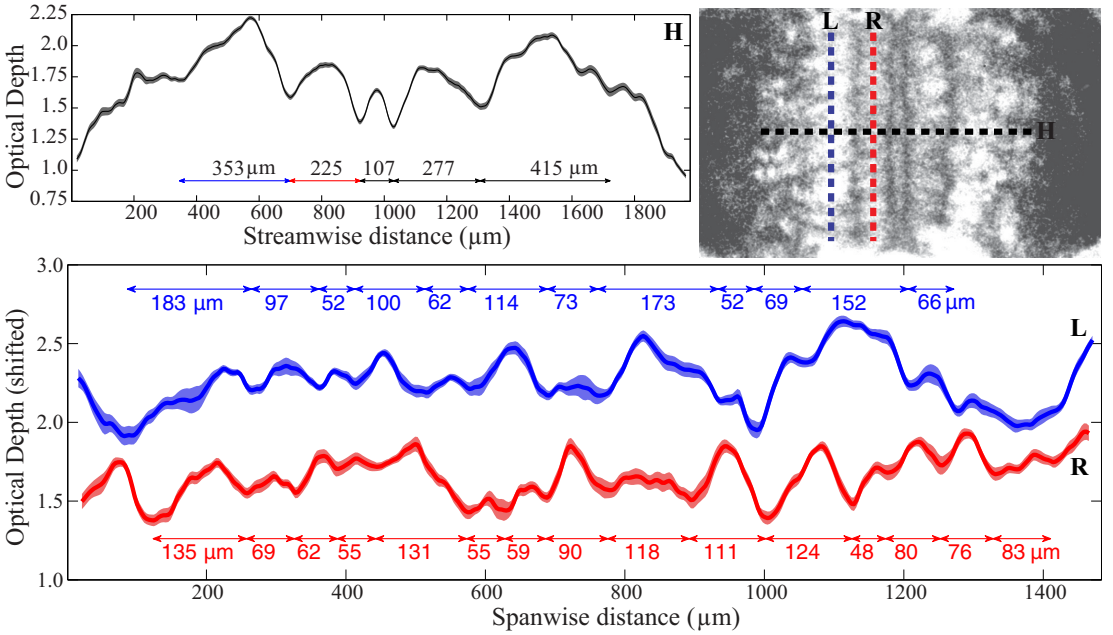

FIG. 4. Lineouts from the titanium data. Top right: Key of lineout locations on the titanium data. Bottom: Two lineouts down the spanwise direction to the left (top line, labeled "L") and right (bottom, "R") of one of the visible rollers. Values of the top lineout are shifted vertically to prevent overlap of the lines. Top left: Lineout in the streamwise direction ("H"). Noise is shown as the shaded envelope along each lineout. Distances between coherent structures visible as low transmission regions (significant local minima in the lineouts) are called out with arrows.

shear-stabilized region, may also play a role in the evolution of the rollers, as they evidently must themselves contain some circulation in some distribution. More exact analysis will depend on modeling the effect of these boundaries in the future.

Estimating as above a Reynolds number from the 34-ns titanium plan view, the early-time circulation per point is 33×10^3 μm^2/ns (as the vorticity is initially distributed over a larger initial number of rollers), but the viscosity is lower and we obtain a Reynolds number estimate of 7×10^7. Again, this is intermediate between the bounding values in Table I implied by the geometry of the experiment. If, however, we take $a = 384$ μm (the mean spacing of the outermost two rollers) and interpret this as a merged, second-generation roller, we have a correspondingly higher Γ and find $\mathrm{Re} = 1.7 \times 10^8$, which agrees closely with our geometric upper limit, which was also estimated for this late time in the experiment.

B. Spanwise filament analysis

Physically, the spanwise secondary instability breaks spanwise symmetry and drives regions alternately upward and downward out of the layer, as was imaged by Jimenez *et al.* [70]. Since the radiograph of this experiment is insensitive to the sign of the velocities (or indeed to the velocity at all), it sees disruption of the interface at twice the spatial period; that is, a ratio of span instability to Kelvin-Helmholtz instability wavelengths $\lambda_{\mathrm{span}}/\lambda_{\mathrm{KH}} = 2/3$ (as measured by Huang and Ho [12]) would appear in our data as a ratio of ratio of 3:1 spanwise to streamwise counts of vortex filaments.

The titanium plan data in Fig. 3 was analyzed with this in mind. Using the spanwise lineouts in Fig. 4, identifying local minima as structures, we find to the left of the roller an average filament spacing b of 98 μm with a spread in measurements of ± 45 μm, and to the right of the roller 86 ± 30 μm. This analysis is repeated for other lineouts and can be found in Fig. 5. We discover fitting across both experiments a vortex spacing ratio a/b of 3.1 ± 0.1 captures the central bulk of the points but fails to describe the titanium outliers, while a fitted quadratic ratio of $b^2/a = 28$ roughly encompasses all points within the quality of measurement. As we shall see later, this second ratio appears in our equation for inferred energy in the mixing layer.

The length scales of spanwise structure thus measured can then be connected to further physical quantities via the elliptical instability which generates them. When the elliptical instability of two vortex filaments developing

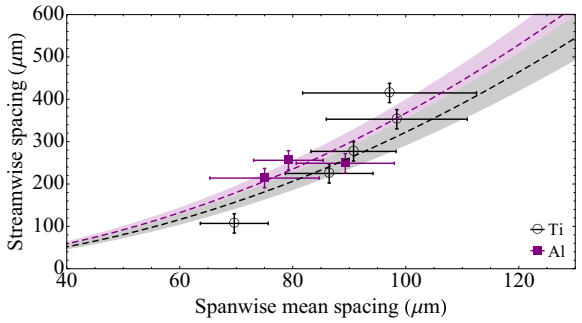

FIG. 5. Measured spanwise filament spacing b (error reported from variance in the measured spacings) vs measured streamwise vortex spacing a (error reported from the 32-μm geometric resolution limit). The dashed lines (with uncertainty bands from the quality of fit) shows $b^2/a = 31 \pm 4$ μm for Ti and 27 ± 3 μm for Al. Open circle data come from titanium shot N150604, filled square data from aluminum shot N150527.

short-wavelength perturbations due to their mutual interaction was experimentally measured [71], it was found to onset with a wavelength of 3.1 times the vortex core size δ. This is consistent with the highest growth rate unstable mode calculated theoretically by Eloy and Le Dizès [68], who obtained a ratio of core size to wavelength of 3.2. Using the value of 3.2 as a correlation between core size and spanwise wavelength and recalling that the true wavelength of the velocity perturbation is twice the observable filament spacing so that $2b = 3.2\delta$, we infer for the aluminum data a typical core size δ of 51 ± 5 μm.

The time evolution and origin of this vortex core can then be investigated. For a vortex with a Lamb-Oseen viscous profile, the core size δ evolves in time by diffusion ν as [72]

$$\left(\frac{2b}{3.2}\right)^2 = \delta^2 = 4\nu t. \tag{1}$$

From the physical plasma viscosities calculated above, we obtain an estimate of elapsed time t required for the layer to evolve from a line of point vortices to the observed value to be 100 μs, which is much longer than the lifetime of the experiment.

Since the irrotational core is thus unlikely to have had time to evolve due to molecular viscosity, at the high inferred Reynolds numbers we encountered earlier it is natural to consider whether small-scale turbulent mixing could be responsible. If the actual time available is around 10 ns, we can calculate from (1) a necessary diffusive term $\nu_\tau = 41$ μm^2/ns. We can interpret this as an eddy viscosity in, for example, a conventional $k-\epsilon$ model such as in Launder and Spalding [73],

$$\nu_\tau = C_\mu \frac{k^2}{\epsilon}, \tag{2}$$

where $C_\mu = 0.09$, k is the turbulent kinetic energy, and ϵ is the dissipation. If we further assume the typical closure for a shear layer (a summary of references can be found in Pope [74]),

$$\frac{Sk}{\epsilon} = 6.0, \tag{3}$$

where S is the strain rate, then for these experiments (where S is of order 1 ns^{-1}) we can combine these results to obtain an estimate of the turbulent specific energy k:

$$k = \frac{S\delta^2}{24 C_\mu t} \approx 1.7 \times 10^{12} \frac{\text{cm}^2}{s^2}. \tag{4}$$

The k thus inferred is a high value in absolute terms, but the normalized value $k/\Delta U^2$ is only about 2×10^{-3}, which is low compared to typical mixing layer conversion efficiencies for incompressible flows, where it is around 0.03 [75, p. 150]. This point will be discussed in the following section.

This has assumed that the rollers visible in the 30.5-ns aluminum data are all first generation and effectively interchangeable. For the titanium data, in which roller amalgamation has occurred near the edges of the image, it is necessary to consider that the core size δ will increase by amalgamation as well as by diffusion of vorticity. Following Landman and Saffman [66], a prototypical merger will double the streamwise distance a and will combine the core areas for an increase in δ of $\sqrt{2}$. In general, we will say that core size has increased by nondiffusive effects by $\sqrt{a_0/a}$, where a_0 is the first-generation roller spacing, identified following the discussion in Sec. IV A as 240 μm for aluminum (taken from the mean streamwise observations) and 107 μm for titanium (taken in the absence of any other information from the smallest visible spacing), and a is the again the instantaneous roller spacing measured to either side of the spanwise lineout. Expressing core size in terms of the spanwise spacing b,

$$\delta = \left(\frac{2}{3.2}\right)\left(\frac{a_0}{a}\right) b, \tag{5}$$

where the 2 comes from the necessary doubling of b to find the actual secondary instability wavelength, and 3.2 is the predicted and measured wavelength-to-core-size ratio. Combining these effects, we finally infer for the titanium data

$$k = \frac{Sb^2(a_0/a)}{3.2^2 \times 6 \times C_\mu t} \approx 4.5 \times 10^{11} \frac{\text{cm}^2}{s^2}. \tag{6}$$

Numerical details including error budget are in Appendix B. We can see in Fig. 6 that this value of k is consistent across all the titanium measurements, despite some very different values of a and b. This is equivalent to the observation that in Fig. 5 all of the titanium points are consistent with a common b^2/a parabola. In Fig. 6 we we can also see that the combined aluminum and titanium streamwise spacing data cluster into groups consistent with first and second generations of merged rollers; the wavelengths normalized by the initial metal foil thicknesses are comparable to the classical solutions of Lord Rayleigh [76] for a mixing layer of initially specified

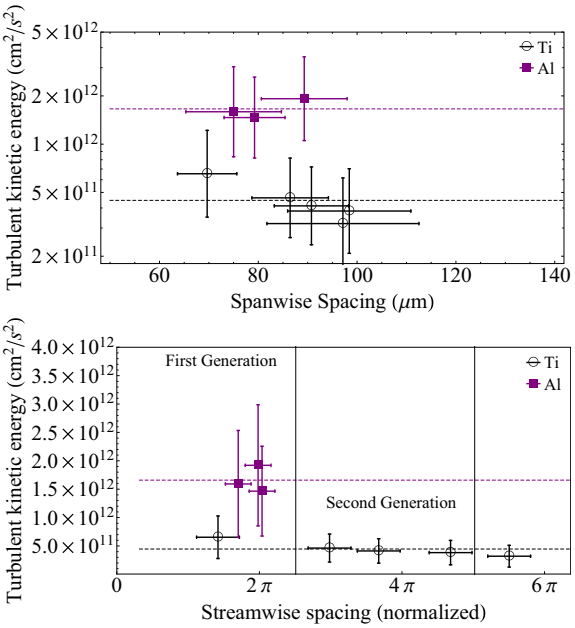

FIG. 6. Turbulent kinetic energies k inferred from lineouts (above) versus the spanwise roller measurements b and (below) versus the local streamwise roller spacing a normalized by the initial widths of the foils (40-μm aluminum and 24-μm titanium). Vertical lines show Rayleigh's solution for finite-thickness mixing layers and its first subharmonic. Points are as in Fig. 5. Horizontal dashed lines show mean inference for each experiment.

width, which suggests a most unstable mode of $\lambda_R \approx 7.9d$, where d is the initial thickness. The agreement is reasonably close, keeping in mind that finer details of density or velocity profiles (which can shorten λ_R by introducing interior length scales) or the dynamic preheat and decompression of the layer before shear (which could increase λ_R by increasing d) will affect the roller spacing in the experiment, and overall is consistent with a mixture of first- and second-generation rollers having progressed by various degrees toward their next merger, shrinking in distance as they do so.

This analysis was made possible by assuming at many stages that the rollers, ribs, and other vortical structures work by analogy to experiments performed in the meters-seconds regime over the years. From those experiments, where fluid variables such as velocity and vorticity could be measured directly, correlations and results established there can now be used under these conditions to infer variables which are difficult to measure directly. With more analysis and experience in using the line-integrated, concentration-sensitive measurements that we obtain, closures such as (3) may soon be replaced with other measurements internal to the experiment.

C. Structure analysis by wavelets

Another approach to this analysis is by the use of transform methods such as Fourier or wavelet decompositions. Due to the strong inhomogeneity of the image and incoherence of the underlying signal of the spanwise instability from one part of the the mixing layer to another, Fourier transforms tend to perform poorly at extracting a length scale from the rest of the features of the image. For images where both spatial and scale degrees of freedom should be retained and separated for the analysis, wavelet transforms are often used in fluid mechanics to extract length scales and orientations of features [77,78]. Using a transform optimized for the particular case of this experiment [79] we can also extract estimates of length scales for our two cases: from the aluminum experiment, 55 μm and 220 μm in the span- and streamwise directions, respectively, and from the titanium experiment 80 μm and 250 μm. (The wavelet transform of the titanium NIF data is shown in Fig. 7.) These lead to energy estimates of 8.5×10^{11} and 3.8×10^{11} cm^2/s^2 respectively. The titanium energy density is close to that obtained by the lineout analysis, and the aluminum energy is lower by half but within the error budget. The greater discrepancy of the aluminum data energy is likely associated with its lower contrast, but overall the wavelet scale analysis is considered a useful check on the overall accuracy of the vortex-counting technique and going forward is expected to prove a useful tool in the analysis of future data.

V. COMPARISON OF ENERGY IN MIXING LAYERS

It is useful to show how the energy values obtained above compare to typical plane mixing layers. The NIF experiments have rare (but not unheard-of) characteristics for a shear mixing layer experiment, most noticeably that it is simultaneously supersonic and possesses high density ratios. Experiments performed in wind tunnels, including Caltech's GALCIT Supersonic Shear Layer Facility [80] or the NASA HYPULSE pulsed-flow wind tunnel [81], have created plane

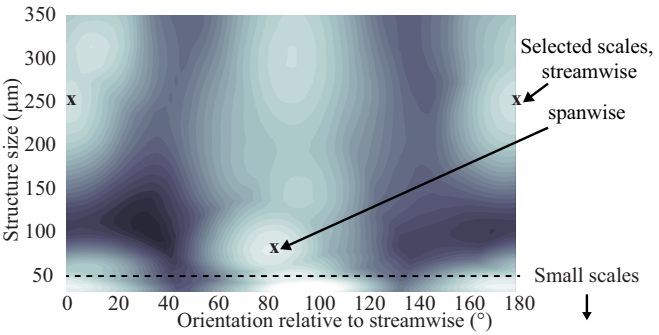

FIG. 7. Scale sizes and orientations detected in the titanium plan view image by anisotropic wavelet transforms. Lighter regions indicate more transform power. The scale axis is bounded on the small side by the resolution. Orientations are continuous across $0^\circ = 180^\circ$. Structure is seen to exist predominantly along the streamwise and spanwise directions, with peak power corresponding to the values used above. Below scales of $\sim$50 μm the power becomes noticeably more isotropic, which may indicate the width of the vortex filament cores or other small-scale structure. The meanings of transform structures such as the excess power at (10°,325 μm) and (90°,325 μm) are the subject of ongoing investigation and may indicate other long-wavelength secondary instabilities or vortex filament curvature.

mixing layers under comparable Mach and Atwood number conditions.

The NIF experiment here is in this section interpreted as a pair of mixing layers between the fast, light sides and the stationary, heavy, metallic plasma in the tube center. This does not change any of the preceding energy analysis, as the layer geometry only explicitly enters through the shear rate $S = L/\Delta U$, which is unchanged here by either considering both L and ΔU to be total values across the layer or by considering them each to be half that. Figure 8 contains the energies previously calculated and normalized against the overall shear flow ΔU. The separate lineouts from common frames of data have been collapsed into averaged points.

The curves in Fig. 8 show scalings following $\sqrt{\rho_{\text{light}}/\rho_{\text{heavy}}}$ in the Atwood direction, and the empirically derived function [82], Eq. (17)

$$0.8 \exp\left(-3M_c^2\right) + 0.2$$

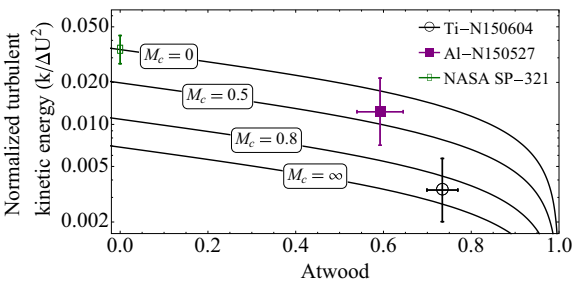

FIG. 8. Turbulent specific kinetic energies normalized by the overall experiment shear flow $k/\Delta U^2$. The square is aluminum NIF data, the circle is titanium NIF data, and the small open rectangle is an aggregate of subsonic experiments reported in NASA SP-321 [84].

performs scaling with compressibility from top to bottom. This density scaling, while heuristic, is the leading order of, for example, the correction to Kelvin-Helmholtz growth rate for variable-density flows [83]. A more complete analysis would be to derive a solution like that derived by Dimotakis [82], Eq. (10) but specialized to the particular geometry of the present experiment.

Figure 8 also contains data from 47 homogenous mixing layer experiments from Birch and Eggers [84] from which the specific normalized turbulent kinetic energy is inferred, which form a cluster of homogenous, subsonic shear experiments in the upper-left. Using results from Townsend [2] on mixing layers which have assumed a self-similar Görtler profile, Townsend's equations (6.5.11), (6.8.8), (6.10.3), and Table 6.3 may be combined to find the turbulent kinetic energy k,

$$\frac{k}{\Delta U^2} = \frac{6.4}{8\sqrt{2\pi}}\left(\frac{1+r}{1-r}\right)\frac{1}{\sigma}, \tag{7}$$

where r is the velocity ratio $U_{\text{slow}}/U_{\text{fast}}$ and σ is the inverse spreading rate of the layer as reported for each experiment in Birch and Eggers [84].

Atwood numbers are assigned by the observed minimum width of the aluminum layer (112 ± 12 μm) measured against the reference density of 2.7 g/cm^3 and initial width of 40 μm when it was assembled. The native titanium density is then inferred by scaling by its native density of 4.5 g/cm^3. From Table I, the usual estimate of convective Mach number, obtained by normalizing against the sum of material sound speeds, $M_c = \Delta U/(c_{s1} + c_{s2}) \simeq 1.1$. In the absence of direct experimental measurements for these speeds, equation-of-state tables are used and the accuracy of this estimate is unknown at present.

Figure 8 shows that the energy estimates thus obtained are reasonable and are broadly consistent with supersonic ($M_c > 0.8$), reasonably high Atwood flow. It is again emphasized that while the normalized values of each of these experiments appear close, and within a region consistent with the rough density and compressibility scaling employed here, the *un-normalized* kinetic energies of the NIF experiment are many times ($\sim 10^{10}$) higher than the conventional, m/s-scale experiments.

VI. SUMMARY

In summary, emergent structures have been observed in the edge-on and plan view measurements of a HED shock-driven shear layer. The velocity differences achieved ($\Delta U =$ 220 km/s) greatly exceed those of conventional mixing layer experiments (e.g., Bell and Mehta [85] $\Delta U = 6$ m/s), high-speed supersonic mixing layer experiments (e.g., Clemens and Mungal [86], $\Delta U = 340$ m/s), and even mixing layer experiments performed in pulsed facilities for supersonic combustion research (e.g., Rosemann, Dimotakis, and Hall [80], $\Delta U \sim 1.3$ km/s; or Erdos [81], $\Delta U = 3.2$ km/s). Taking into account the energy scaling of k as ΔU^2, our absolute specific turbulent kinetic energies are expected to be 10^3 to 10^4 higher than the fastest conventional or pulsed systems. The total energy density ρk of the turbulent field is an equivalent pressure of 100 kbar to 1 Mbar.

While this experiment has additional underlying physics beyond gas- and water-channel experiments due to the presence of the initially solid-density metal layer separating the sides, and the radiation-hydrodynamic loading which melts the materials and drives the shocks which initiate the experiment, the experiments have been analyzed here in the context of and using results applicable to traditional plane mixing layers. Using correlations with primary and secondary coherent structure scales developed for the traditional plane mixing layer, we obtain estimates for turbulence quantities which cannot be measured directly. We obtain broadly consistent results in Reynolds number, vortex ellipticity, and turbulent kinetic energy. As the analysis and further experiments proceed, it is intended that the closures by analogy to conventional shear layers will eventually be replaced by additional measurements on the present system. By doing so, we will uncover, or determine the necessary conditions to bring about, the deviations from conventional behavior due to effects of high density ratios, strong compressibility regions, or plasma effects. This will inform models extrapolated to describe shear-induced mixing at very high k, where such mixing has an impact but is not directly observable, such as in inertial fusion experiments or astrophysical events.

ACKNOWLEDGMENTS

The authors would like to acknowledge the support and involvement of other researchers involved in fabricating, fielding, and interpreting these experiments, including D. Capelli, T. Cardenas, B. DeVolder, J. Fincke, J. Kline, L. Kot, S. Kurien, E. Loomis, T. Perry, D. Schmidt, and C. Di Stefano from Los Alamos National Laboratory; and C. Huntington, S. MacLaren, S. Nagel, H.-S. Park, P. Wang, and Y. Zhou from Lawrence Livermore National Laboratory. Computations in analysis used MATLAB and its Wavelet Toolbox to perform transforms. This work was supported by the U.S. Department of Energy and executed by Los Alamos National Laboratory under Contract No. DE-AC52-06NA25396. Experiments performed on the National Ignition Facility additionally reflect facility development and operations performed under the U.S. Department of Energy by Lawrence Livermore National Laboratory under Contract No. DE-AC52-07NA27344.

APPENDIX A: FLUID PARAMETERS OF THE PLASMA

While the experiment is in a hot, dense plasma state, effective fluid parameters have been estimated based on simulation and theory informed by the measurements of shock velocity. Shock interaction with the wall is visible in a number of shots, which is used to calibrate two-dimensional simulations in the RAGE [60] hydrocode, which in turn provides estimates of postshock pressures and temperatures. The ion viscosity is computed using a formula from Braginskii [87],

$$\rho\nu = 0.96 n_i \tau_i k_B T = 0.96 \frac{3}{4\sqrt{\pi}} \frac{m_i^{1/2}(k_B T)^{5/2}}{Z^4 e^4 \ln\Lambda}, \tag{A1}$$

where n_i is ion number density, τ_i is a collision time, k_B is the Boltzmann constant, and T is the plasma temperature. Galmiche and Gauthier [88] evaluate the component terms for our conditions in cgs units to obtain the second form in which

m_i is the mass of the ion, Z is the ionization level, e is the (Gaussian) electron charge, and $\ln\Lambda$ is a Coulombic logarithm (of order 1) for particle scattering mediated by long-range electromagnetic deflections. Expressions for the component terms can be found in standard references [such as 89]. We evaluate using a T of 50 eV, $\ln\Lambda = 1$, a ρ of 1 g/cm^3 in aluminum, and 2 g/cm^3 in titanium, and other parameters as in Table I. We expect the resulting estimate of ν to be suitably accurate at least for order-of-magnitude calculations such as Reynolds numbers. The viscosity of the plasma-state metals is found to be strongly influenced by the ionization and is correspondingly lower in titanium than in aluminum due to the greater number of loosely bound electrons with ionization thresholds <100 eV.

The sound speeds of the metal layers are estimated by

$$c_s = \sqrt{\gamma(1+Z)Tk_B/(Am_0)}, \tag{A2}$$

where m_0 is the mass of a nucleon and the polytropic index γ is assumed to be 5/3 (producing an upper limit for the speed of sound, and correspondingly, a lower limit for Mach numbers). Table I collects results for the different experiment configurations using a temperature T of 50 eV.

An implication of these calculations is that the mixing layer convective Mach number M_c may be 1 if measured from one foam region to the other, but as high as 3 if measured from one end of the metal layer to the other.

The experiment contains several initial-time length scales which, due to the preparation of the experiment in the solid phase, can be measured in detail prior to the experiment. Of the various dimensions in the experiment, the two most obvious length scales of interest are the dynamic width of the metal foil and its associated mixing layer and the initial roughness of the metal foil. The layer width, which separates the fast-flowing foam on one side of the layer from the other, defines the minimum length which can couple to the maximum amount of shear and can be expected to influence a most-unstable mode in the early system. The roughness, on the other hand, would be expected to interact with the shock and form a proportionally sized premixed region between the foam and the metal. The integral-scale Reynolds number is estimated

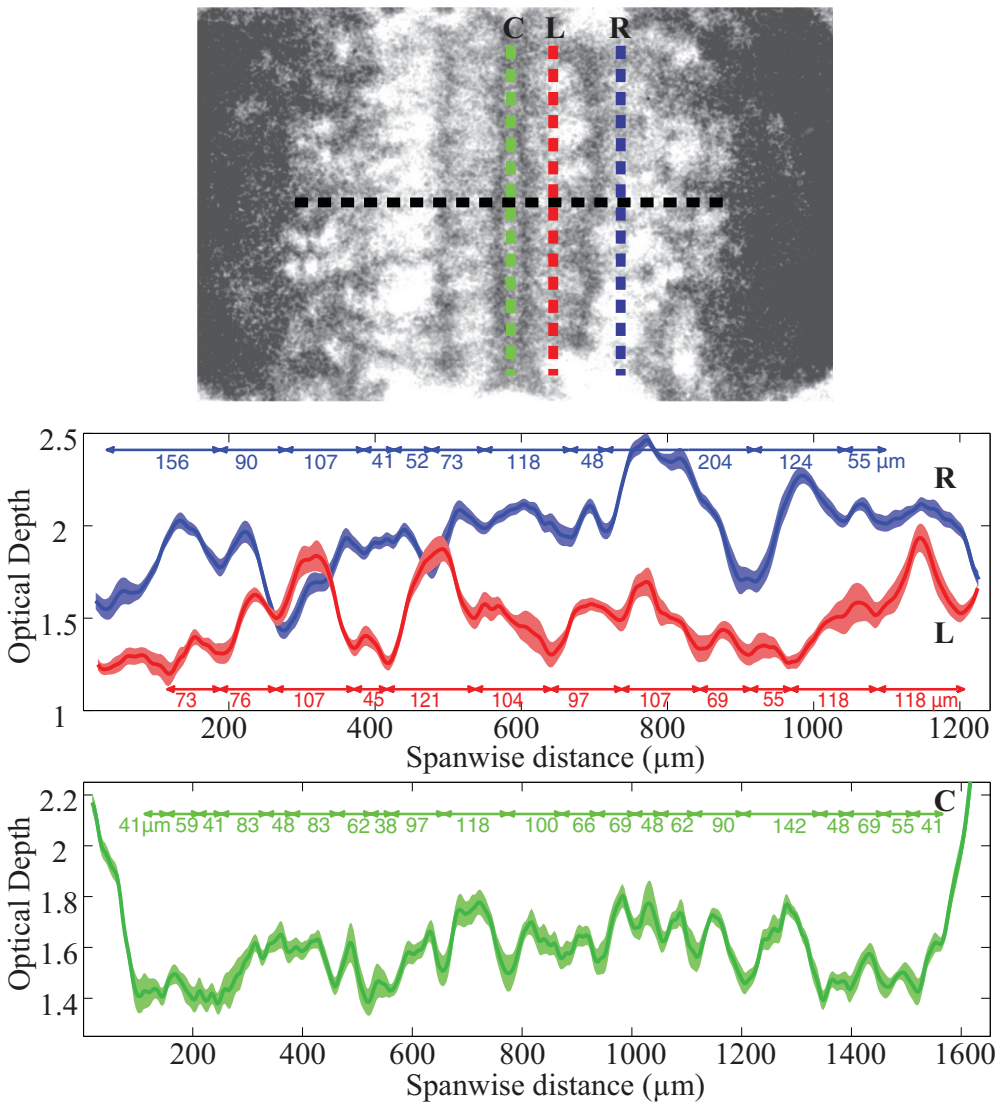

FIG. 9. Other lineouts from the titanium N150604 data analyzed for Fig. 5. These were combined with the analysis of lineouts in Fig. 4.

using the difference in velocity streams, $\Delta U = 220\,\mathrm{km/s}$, and the minimum width of the metal layer, immediately prior to the onset of shear, measured to be approximately 140 μm in aluminum and assumed to be half of that in titanium, proportionate to the initially approximately halved width of the foil during manufacturing.

A roughness-scale Reynolds number is also calculated. The roughness is measured by profilometry prior to the experiment and is found to have a root-mean-square value of 200 nm. This corresponds to length scales which one would expect to be energized by the initial passage of the shock and interaction with the surface. As reported in Merritt *et al.* [90], experiments are also underway in which modifications of the roughness during the machining process are used to control the onset of mixing.

APPENDIX B: ALL LINEOUTS

All lineouts are presented from the titanium (Fig. 9) and aluminum (Fig. 10) data used in constructing Figs. 5 and 6. Calculations of the turbulent kinetic energy using Eq. (6) assumed experimental and model form uncertainties as follows: a,a_0, and b as in Fig. 5. The core-size correlation to a spanwise instability factor of "3.2" was 3.1 ± 0.3 [71]

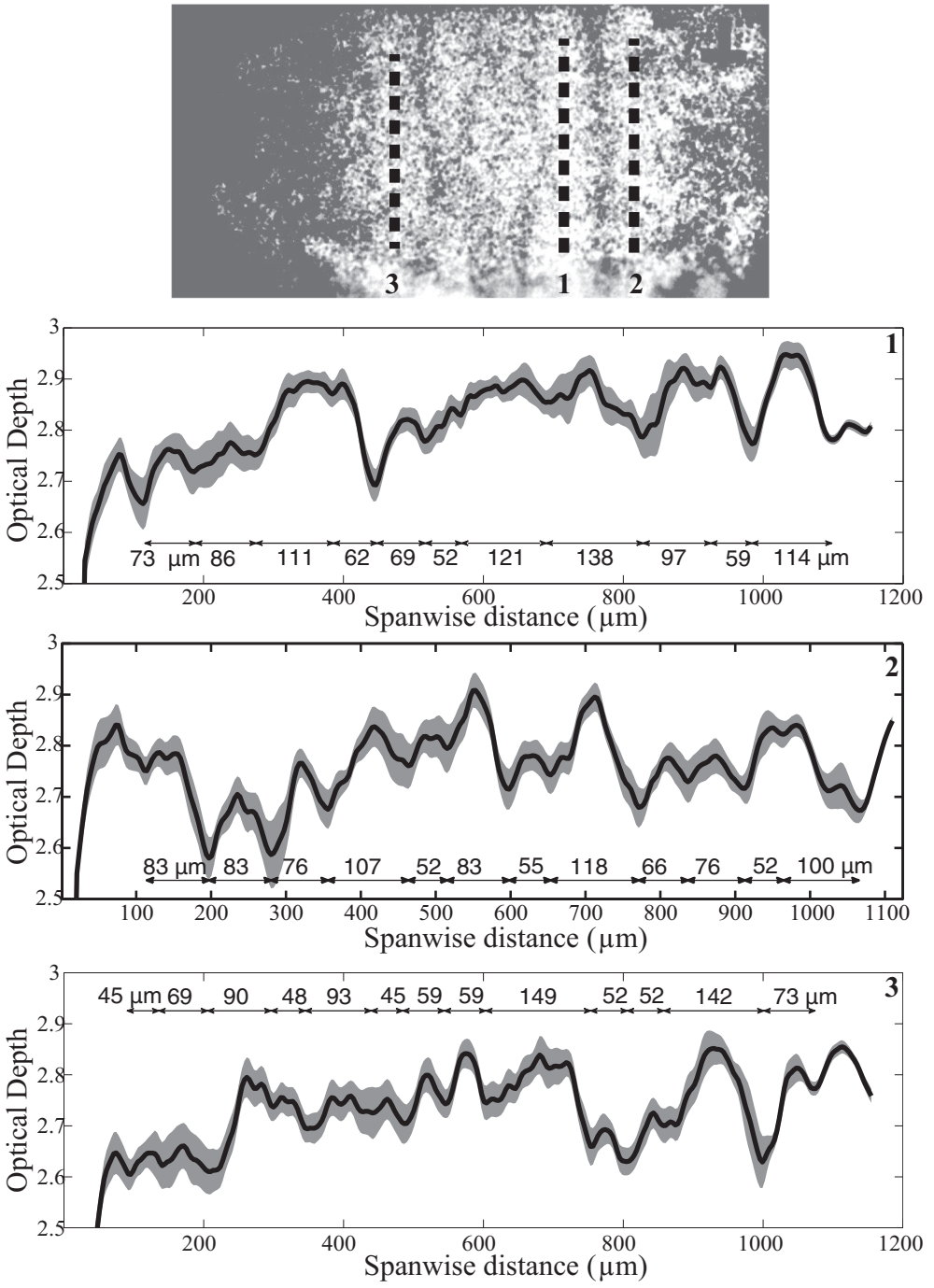

FIG. 10. Lineouts from the aluminum N150527 data analyzed for Fig. 5.

based on experimental error bars. The shear $k-\epsilon$ closure "6" was modeled as 5.5 ± 1 based on values in Pope [74]. The time from shear initiation was taken as the imaging time minus 18 ns (the time of shock crossing) ± 3 ns (to account for uncertainty on whether shear initiates when the shocks enter the central region, when they cross, or when they leave the central region; absolute measurement of the observation time from the time the lasers turn on is known to 1/10 ns). For the shear rate S, the simulated shock-induced shear speed ($\Delta U = 220$ μm/ns) is divided by the instantaneous total mixing layer thickness l (300 ± 25 μm in the aluminum [52], 400 ± 30 μm in the titanium) to obtain a lower limit, as interior variations in the velocity profile would locally raise this value. The most likely values used were 0.86 ns^{-1} with uncertainty ± 0.25 ns^{-1}. No uncertainty was used for the model-closing constant $C_\mu = 0.09$.

[1] W. Thomson, Nature (London) **23**, 45 (1880).
[2] A. A. Townsend, *The Structure of Turbulent Shear Flow*, 2nd ed. (Cambridge University Press, Cambridge, UK, 1976).
[3] M. M. Koochesfahani and P. E. Dimotakis, J. Fluid. Mech **170**, 83 (1986).
[4] R. D. Mehta, Exp. Fluids **10**, 194 (1991).
[5] G. L. Brown and A. Roshko, J. Fluid Mech. **64**, 775 (1974).
[6] D. W. Bogdanoff, AIAA J. **21**, 926 (1983).
[7] D. Papamoschou and A. Roshko, J. Fluid. Mech **197**, 453 (1988).
[8] F. K. Browand, J. Fluid. Mech **26**, 281 (1966).
[9] R. Breidenthal, J. Fluid. Mech **109**, 1 (1981).
[10] L. P. Bernal and A. Roshko, J. Fluid. Mech **170**, 499 (1986).
[11] J. Jimenez, J. Fluid. Mech **132**, 319 (1983).
[12] L. Huang and C. Ho, J. Fluid Mech. **210**, 475 (1990).
[13] J. H. Bell and R. D. Mehta, J. Fluid Mech. **239**, 213 (1992).
[14] O. Zeman, Phys. Fluids A **2**, 178 (1990).
[15] D. C. Wilcox, AIAA J. **30**, 2639 (1992).
[16] M. F. Barone, W. L. Oberkampf, and F. G. Blottner, AIAA J. **44**, 1488 (2006).
[17] V. A. Smalyuk, R. E. Tipton, J. E. Pino, D. T. Casey, G. P. Grim, B. A. Remington, D. P. Rowley, S. V. Weber, M. Barrios, L. R. Benedetti *et al.*, Phys. Rev. Lett. **112**, 025002 (2014).
[18] D. T. Casey, V. A. Smalyuk, R. E. Tipton, J. E. Pino, G. P. Grim, B. A. Remington, D. P. Rowley, S. V. Weber, M. Barrios, L. R. Benedetti *et al.* Phys. Plasmas **21**, 092705 (2014).
[19] W. D. Arnett, C. Meakin, M. Viallet, S. W. Campbell, J. C. Lattanzio, and M. Mocák, Astrophys. J. **809**, 30 (2015).
[20] D. Papamoschou, Phys. Fluids **7**, 233 (1995).
[21] F. S. Alvi, A. Krothapalli, and D. Washington, AIAA J. **34**, 728 (1996).
[22] T. A. Ninnemann and W. F. Ng, Exp. Fluids **13**, 98 (1992).
[23] P. J. Strykowski and D. L. Niccum, Phys. Fluids A **4**, 770 (1992).
[24] Y. B. Zeldovich and Y. P. Razier, *Physics of Shock Waves and High-Temperature Hydrodynamic Phenomena* (Academic Press, New York, 1967).
[25] S. Atzeni and J. Meyer-ter-Vehn, *The Physics of Inertial Fusion: Beam Plasma Interaction, Hydrodynamics, Hot Dense Matter* (Clarendon Press, Oxford, UK, 2004).
[26] R. P. Drake, *High-Energy-Density Physics* (Springer, New York, 2006).
[27] J. Colvin and J. Larsen, *Extreme Physics: Properties and Behavior of Matter at Extreme Conditions* (Cambridge University Press, Cambridge, UK, 2014).
[28] B. A. Remington, R. P. Drake, and D. D. Ryutov, Rev. Mod. Phys. **78**, 755 (2006).
[29] A. J. Cole, J. D. Kilkenny, P. T. Rumsby, R. G. Evans, C. J. Hooker, and M. H. Key, Nature (London) **299**, 329 (1982).
[30] S. G. Glendinning, S. V. Weber, P. Bell, L. B. DaSilva, S. N. Dixit, M. A. Henesian, D. R. Kania, J. D. Kilkenny, H. T. Powell, R. J. Wallace, P. J. Wegner, J. P. Knauer, and C. P. Verdon, Phys. Rev. Lett. **69**, 1201 (1992).
[31] H. F. Robey, Phys. Plasmas **11**, 4123 (2004).
[32] C. C. Kuranz, R. P. Drake, M. J. Grosskopf, B. Fryxell, A. Budde, J. F. Hansen, A. R. Miles, T. Plewa, N. Hearn, and J. Knauer, Phys. Plasmas **17**, 052709 (2010).
[33] J. S. Wark, J. D. Kilkenny, A. J. Cole, M. H. Key, and P. T. Rumsby, Appl. Phys. Lett. **48**, 969 (1986).
[34] K. S. Raman, V. A. Smalyuk, D. T. Casey, S. W. Haan, D. E. Hoover, O. A. Hurricane, J. J. Kroll, A. Nikroo, J. L. Peterson, B. A. Remington, H. F. Robey, D. S. Clark, B. A. Hammel, O. L. Landen, M. M. Marinak, D. H. Munro, K. J. Peterson, and J. Salmonson, Phys. Plasmas **21**, 072710 (2014).
[35] B. A. Hammel, J. D. Kilkenny, D. Munro, B. A. Remington, H. N. Kornblum, T. S. Perry, D. W. Philion, and R. J. Wallace, Phys. Plasmas **1**, 1662 (1994).
[36] O. A. Hurricane, J. F. Hansen, H. F. Robey, B. A. Remington, M. J. Bono, E. C. Harding, R. P. Drake, and C. C. Kuranz, Phys. Plasmas **16**, 056305 (2009).
[37] E. C. Harding, J. F. Hansen, O. A. Hurricane, R. P. Drake, H. F. Robey, C. C. Kuranz, B. A. Remington, M. J. Bono, M. J. Grosskopf, and R. S. Gillespie, Phys. Rev. Lett. **103**, 045005 (2009).
[38] C. A. Di Stefano, G. Malamud, M. T. H. de Frahan, C. C. Kuranz, A. Shimony, S. R. Klein, R. P. Drake, E. Johnsen, D. Shvarts, V. A. Smalyuk, and D. Martinez, Phys. Plasmas **21**, 056306 (2014).
[39] W. C. Wan, G. Malamud, A. Shimony, C. A. Di Stefano, M. R. Trantham, S. R. Klein, D. Shvarts, C. C. Kuranz, and R. P. Drake, Phys. Rev. Lett. **115**, 145001 (2015).
[40] L. Welser-Sherrill, J. Fincke, F. Doss, E. Loomis, K. Flippo, D. Offermann, P. Keiter, B. Haines, and F. Grinstein, High Energy Density Physics **9**, 496 (2013).
[41] O. A. Hurricane, V. A. Smalyuk, K. Raman, O. Schilling, J. F. Hansen, G. Langstaff, D. Martinez, H.-S. Park, B. A. Remington, H. F. Robey, J. A. Greenough, R. Wallace, C. A. Di Stefano, R. P. Drake, D. Marion, C. M. Krauland, and C. C. Kuranz, Phys. Rev. Lett. **109**, 155004 (2012).
[42] V. A. Smalyuk, J. F. Hansen, O. A. Hurricane, G. Langstaff, D. Martinez, H.-S. Park, K. Raman, B. A. Remington, H. F. Robey, O. Schilling, R. Wallace, Y. Elbaz, A. Shimony, D. Shvarts, C. Di Stefano, R. P. Drake, D. Marion, C. M. Krauland, and C. C. Kuranz, Phys. Plasmas **19**, 092702 (2012).
[43] V. A. Smalyuk, O. A. Hurricane, J. F. Hansen, G. Langstaff, D. Martinez, H.-S. Park, K. Raman, B. A. Remington, H. F. Robey, O. Schilling, R. Wallace, Y. Elbaz, A. Shimony, D. Shvarts, C. Di Stefano, R. P. Drake, D. Marion, C. M. Krauland, and C. C. Kuranz, High Energy Density Phys. **9**, 47 (2013).

[44] P. Chassaing, R. A. Antonia, F. Anselmet, L. Joly, and S. Sarkar, *Variable Density Fluid Turbulence*, Fluid Mechanics and its Applications No. 69 (Kluwer Academic Publishers, Dordrecht, 2002).

[45] D. C. Besnard, F. H. Harlow, and R. M. Rauenzahn, Los Alamos National Laboratory Report No. LA-10911-MS, 1987.

[46] S. Gauthier and M. Bonnet, Phys. Fluids A **2**, 1685 (1990).

[47] O. Grégoire, D. Souffland, and S. Gauthier, J. Turbulence **6**, N29 (2005).

[48] G. Dimonte and R. Tipton, Phys. Fluids **18**, 085101 (2006).

[49] J. D. Schwarzkopf, D. Livescu, J. R. Baltzer, R. A. Gore, and J. R. Ristorcelli, Flow, Turbul. and Combust. **96**, 1 (2016).

[50] C. A. Kennedy and T. B. Gatski, Phys. Fluids **6**, 662 (1994).

[51] A. Banerjee, R. A. Gore, and M. J. Andrews, Phys. Rev. E **82**, 046309 (2010).

[52] F. W. Doss, J. L. Kline, K. A. Flippo, T. S. Perry, B. G. DeVolder, I. Tregillis, E. N. Loomis, E. C. Merritt, T. J. Murphy, L. Welser-Sherrill, and J. R. Fincke, Phys. Plasmas **22**, 056303 (2015).

[53] K. A. Flippo, F. W. Doss, B. Devolder, J. R. Fincke, E. N. Loomis, J. L. Kline, and L. Welser-Sherrill, J. Phys.: Conf. Ser. **688**, 012018 (2016).

[54] T. R. Boehly, D. L. Brown, R. S. Craxton, R. L. Keck, J. P. Knauer, J. H. Kelly, T. J. Kessler, S. A. Kumpan, S. J. Loucks, S. A. Letzring, F. J. Marshall, R. L. McCrory, S. F. B. Morse, W. Seka, J. M. Soures, and C. P. Verdon, Opt. Commun. **133**, 495 (1997).

[55] F. W. Doss, J. R. Fincke, E. N. Loomis, L. Welser-Sherrill, and K. A. Flippo, Phys. Plasmas **20**, 122704 (2013).

[56] F. W. Doss, E. N. Loomis, L. Welser-Sherrill, J. R. Fincke, K. A. Flippo, and P. A. Keiter, Phys. Plasmas **20**, 012707 (2013).

[57] E. Loomis, F. Doss, K. Flippo, and J. Fincke, Phys. Plasmas **21**, 044508 (2014).

[58] E. I. Moses and C. R. Wuest, Fusion Sci. Technol. **43**, 420 (2003).

[59] J. Lindl, Phys. Plasmas **2**, 3933 (1995).

[60] M. Gittings, R. Weaver, M. Clover, T. Betlach, N. Byrne, R. Coker, E. Dendy, R. Hueckstaedt, K. New, W. R. Oakes, D. Ranta, and R. Stefan, Comput. Sci. Discovery **1**, 015005 (2008).

[61] S. P. Lyon and J. D. Johnson, SESAME: The Los Alamos National Laboratory Equation of State Database, Report No. LA-UR-92-3407, 1992.

[62] K. A. Flippo, J. L. Kline, F. W. Doss, E. N. Loomis, M. Emerich, B. Devolder, T. J. Murphy, K. B. Fournier, D. H. Kalantar, E. Merritt, T. S. Perry, I. Tregillis, L. Welser-Sherrill, and J. R. Fincke, Rev. Sci. Instrum. **85**, 093501 (2014).

[63] R. T. Pierrehumbert and S. E. Widnall, J. Fluid. Mech **114**, 59 (1982).

[64] R. T. Pierrehumbert, Phys. Rev. Lett. **57**, 2157 (1986).

[65] B. J. Bayly, Phys. Rev. Lett. **57**, 2160 (1986).

[66] M. J. Landman and P. G. Saffman, Phys. Fluids **30**, 2339 (1987).

[67] F. Waleffe, Phys. Fluids A **2**, 76 (1990).

[68] C. Eloy and S. Le Dizès, J. Fluid. Mech **378**, 145 (1999).

[69] P. E. Dimotakis, J. Fluid. Mech **409**, 69 (2000).

[70] J. Jimenez, M. Cogollos, and L. P. Bernal, J. Fluid Mech. **152**, 125 (1985).

[71] P. Meunier and T. Leweke, Phys. Fluids **13**, 2747 (2001).

[72] E. Meiburg and P. K. Newton, J. Fluid. Mech **227**, 211 (1991).

[73] B. E. Launder and D. B. Spalding, Comput. Methods Appl. Mech. Eng. **3**, 269 (1974).

[74] S. B. Pope, *Turbulent Flows* (Cambridge University Press, Cambridge, UK, 2000).

[75] A. Smits and J.-P. Dussage, *Turbulent Shear Layers in Supersonic Flow* (Springer, New York, 2006).

[76] Lord Rayleigh, Proc. London Math. Soc. **s1–11**, 57 (1880).

[77] M. Farge, Annu. Rev. Fluid Mech. **24**, 395 (1992).

[78] J.-P. Antoine, P. Carrette, R. Murenzi, and B. Piette, Signal Process. **31**, 241 (1993).

[79] E. C. Merritt and F. W. Doss, Rev. Sci. Instrum. **87**, 075103 (2016).

[80] H. Rosemann, P. Dimotakis, and J. L. Hall, in *Eddy Structure Identification in Free Turbulent Shear Flows*, edited by J. P. Bonnet and M. N. Glauser (Kluwer Academic, Dordrecht, 1993).

[81] J. I. Erdos, in *Combustion in High Speed Flows*, edited by J. Buckmaster, T. L. Jackson, and A. Kumar (Kluwer Academic, Dordrecht, 1994).

[82] P. Dimotakis, in *High-Speed Flight Propulsion Systems*, edited by E. T. Curran and S. N. B. Murphy, Progress in Astronautics and Aeronautics Vol. 137 (AIAA, Reston, VA, 1991), p. 265.

[83] G. Taylor, Proc. R. Soc. London A **132**, 499 (1931).

[84] S. F. Birch and J. M. Eggers, in *Free Turbulent Sheer Flows*, Vol. 1 (Scientific and Technical Information Office, NASA, Washington DC, 1973).

[85] J. H. Bell and R. D. Mehta, AIAA J. **28**, 2034 (1990).

[86] N. T. Clemens and M. G. Mungal, Exp. Fluids **11**, 175 (1991).

[87] S. I. Braginskii, in *Reviews of Plasma Physics*, Vol. 1, edited by M. A. Leontovich (Consultants Bureau, New York, 1965).

[88] D. Galmiche and S. Gauthier, Jpn. J. Appl. Phys. **35**, 4516 (1996).

[89] J. D. Huba, *NRL Plasma Formulary* (Naval Research Laboratory, Washington DC, 2011).

[90] E. C. Merritt, F. W. Doss, E. N. Loomis, K. A. Flippo, and J. L. Kline, Phys. Plasmas **22**, 062306 (2015).